CO_2 Photoreduction

DOI: 10.1002/ange.201409183

Photocatalytic Reduction of Carbon Dioxide by Hydrous Hydrazine over Au–Cu Alloy Nanoparticles Supported on $SrTiO_3/TiO_2$ Coaxial Nanotube Arrays**

*Qing Kang, Tao Wang, Peng Li, Lequan Liu, Kun Chang, Mu Li, and Jinhua Ye**

Abstract: *Efficient photocatalytic conversion of CO_2 into CO and hydrocarbons by hydrous hydrazine ($N_2H_4{\cdot}H_2O$) is achieved on $SrTiO_3/TiO_2$ coaxial nanotube arrays loaded with Au–Cu bimetallic alloy nanoparticles. The synergetic catalytic effect by the Au–Cu alloy nanoparticles and the fast electron-transfer in $SrTiO_3/TiO_2$ coaxial nanoarchitecture are the main reasons for the efficiency, while $N_2H_4{\cdot}H_2O$ as the H source and electron donor provides a reducing atmosphere to protect the surface Cu atoms from oxidation, therefore maintaining the alloying effect which is the basis for the high photocatalytic activity and stability. This approach opens a feasible route to enhance the photocatalytic efficiency, which also benefits the development of photocatalysts and co-catalysts.*

Hydrocarbon fuels are currently the most important source of energy due to their ready availability, stability, and high energy density.[1] Solar-energy-driven conversion of CO_2 into hydrocarbon fuels can simultaneously generate chemical fuels to meet energy demand and mitigate rising CO_2 levels.[2] The utilization of the clean and renewable solar power resource is, on a long-term basis, an essential component of solutions to address growing global energy demand.[2] Since Halmann discovered the photoelectrochemical reduction of CO_2 into organic compounds in 1978,[3] a growing interest in the development of semiconductor photocatalysts has evolved. To date, over 130 kinds of photocatalysts have been investigated to catalyze the CO_2 reduction.[4] Among them, strontium titanate ($SrTiO_3$, STO) and titania (TiO_2) are two of the most investigated photocatalytic materials.[4a,5] Since their high conduction band position, they are expected to have enough energy to participate in the multielectron and multiproton processes for reducing CO_2. Scheme S1 in the Supporting Information shows the conduction band, valence-band potentials, and band-gap energies of STO and TiO_2 relative to the redox potentials at pH 7 of compounds involved in CO_2 reduction. Although the STO and TiO_2 cannot provide sufficient potential to transfer a single photogenerated electron to a free CO_2 molecule (-1.9 V_{NHE}),[4a] the conduction band of STO and TiO_2 are much higher than the electrochemical reduction potentials of CO_2 into formic acid, carbon monoxide, formaldehyde, methanol, and methane. This means that the multielectron and multiproton reactions are feasible. Moreover, benefiting from the favorable energy-band position, developing STO/TiO_2 heterostructure for better charge separation is an effective strategy to improve the photocatalytic activity. Previous work reported that the more contact between STO and TiO_2, the better the photocatalytic activity.[6] Therefore, close contact between STO and TiO_2 is necessary when designing a heterostructure with a good photocatalytic performance.

One-dimensional (1D) nanomaterials with various morphologies, such as nanotube, nanowire, and nanorod, owing to their large surface areas, have been demonstrated to facilitate the electron transport and to minimize the loss of charge carriers at grain boundaries.[7] Among the 1D nanostructures, highly ordered vertical TiO_2 nanotube arrays (NTAs) have shown the significant photocatalytic activity of CO_2 reduction.[2,8] However, maintaining the long-time stability and high activity of the catalyst, especially the co-catalyst, is still a great challenge. Noble-metal Pt nanoparticles (NPs) are easily poisoned by CO during the catalytic process[9] and for non-noble metal NPs, changes of surface states[10] is the main reason for the co-catalyst deactivation.

Herein, we develop a new approach that is able to achieve high-rate UV/Vis-light-driven conversion of diluted CO_2 into CO and hydrocarbons in which STO/TiO_2 coaxial nanotube arrays loaded with an optimized combination of Au–Cu bimetallic NPs are used as the photocatalyst. Under UV/Vis-light illumination, a CO production rate of 138.6 ppm cm^{-2} h^{-1} (3.77 mmol g^{-1} h^{-1}) and total hydrocarbon production rate of 26.68 ppm cm^{-2} h^{-1} (725.4 μmol g^{-1} h^{-1}) are obtained on Au_3Cu@$SrTiO_3/TiO_2$ nanotube arrays by using diluted CO_2 (33.3 % in Ar). Generally the highest rate of production (e.g. methane) in previous reports does not exceed tens of μmol per hour of illumination per gram of photocatalyst.[4a,11] The key improvement is the effectiveness of our photocatalyst owing to following strategies: 1) employing high surface area nanotube array architectures, with holes in the tube walls to

[*] Dr. Q. Kang, Dr. T. Wang, Dr. P. Li, Dr. L. Liu, Dr. K. Chang, Prof. J. Ye
International Center for Materials Nanoarchitectonics (MANA), and Environmental Remediation Materials Unit
National Institute for Materials Science (NIMS)
1-1 Namiki, Tsukuba, Ibaraki 305-0044 (Japan)
M. Li, Prof. J. Ye
Graduate School of Chemical Science and Engineering
Hokkaido University, Sapporo 060-0814 (Japan)
E-mail: Jinhua.YE@nims.go.jp
Prof. J. Ye
TU-NIMS Joint Research Center, School of Material Science and Engineering, Tianjin University
92 Weijin Road, Tianjin (P.R. China)

[**] This work received financial support from the World Premier International Research Center Initiative (WPI Initiative) on Materials Nanoarchitectonics (MANA), MEXT (Japan), and National Basic Research Program of China (973 Program, 2014CB239301).

Supporting information for this article is available on the WWW under http://dx.doi.org/10.1002/anie.201409183.

enhance the gas diffusion and increase the contact between photogenerated charge carriers and surface species; 2) developing STO/TiO_2 heterostructures to facilitate the photogenerated charge separation; 3) distributing noble bimetallic alloy NPs co-catalysts along the nanotube arrays to help the redox process; and 4) choosing hydrous hydrazine ($N_2H_4{\cdot}H_2O$) as H source and electron donor to provide a reductive atmosphere for keeping the alloying effect.

For fabrication of the STO/TiO_2 coaxial nanotube arrays, TiO_2 nanotube arrays were first prepared by anodic oxidation. The amorphous TiO_2 was converted into STO by a hydrothermal method. Then Au–Cu bimetallic alloy NPs with different Au/Cu ratios were deposited on the STO/TiO_2 nanotube arrays by a microwave-assisted solvothermal method. The carbon residue was removed by annealing. Full details are given in the Supporting Information.

The morphologies of the nanotube array photocatalysts are shown in SEM images (Figure 1 A and Supporting Information Figure S1). The amorphous TiO_2 nanotube arrays obtained by anodic oxidation are approximately 110 nm in diameter and 30 μm in length. After the hydrothermal process, a part of TiO_2 changes to STO, causing the wall thickness to increase and thus the corresponding diameter decreases to 100 nm. In addition, the length decreases to 20 μm. Closer observations in Figure 1 A shows there are plenty holes (as indicated by arrows) in the tube wall, which are beneficial for the gas flow diffusion and facilitate the contact between the charge carriers and the surface species. The X-ray diffraction (XRD) pattern in Figure 1 B confirms the existence of STO. Since unchanged TiO_2 is amorphous, the XRD pattern does not show the TiO_2 peaks in the fresh STO/TiO_2 sample. The top-view and cross-sectional energy dispersive X-ray spectroscopy (EDX) mappings (Figure S2) verify that the Au_3Cu NPs are uniformly distributed on the surface of the STO/TiO_2 nanotube arrays and the Au_3Cu coating exists throughout the length of the nanotube arrays. Furthermore, the cross-section SEM image and EDX mappings confirm that the STO/TiO_2 is a coaxial nanotube structure. After annealing, the amorphous TiO_2 are annealed to anatase, which is confirmed by the XRD pattern (Figure 1 B). Figure 1 C shows a typical TEM image of the Au_3Cu@STO/TiO_2 nanotube arrays. It can be seen that small alloy NPs are uniformly dispersed on the support. The average diameter of the Au_3Cu, Au_2Cu_2, and $AuCu_3$ NPs is calculated to be 5.14, 6.62, and 7.78 nm, respectively, indicating that the ratio of Au/Cu affects the size of the bimetal alloy NPs (Figure S3). HRTEM image (Figure 1 D) shows the Au_3Cu bimetallic NPs is indexed as a face-centered cubic (fcc) cuboctahedron structure. The characterization of the alloy phase is supported by the fast Fourier transform (FFT) pattern (Figure 1 D, Inset). The lattice constants calculated from the lattice spacing of the alloy NPs ($a = 0.396$ nm) is between the lattice constants for standard Au (JCPDS 04-0784, $a = 0.4079$ nm) and Cu (JCPDS 04-0836, $a = 0.3615$ nm), and is similar to the value calculated based on Vegard's law ($a = 0.3955$ nm).[10] The result suggests that the Au and Cu components in the alloy are homogeneously mixed. As shown in Figure S4, the diffuse-reflectance UV/Vis spectrum of the Au@STO/TiO_2 nanotube arrays shows a distinctive surface plasmon resonance (SPR) band at 570 nm. Cu alloying decreases the SPR intensity with a red shift of the band, as is the case for colloidal Au–Cu alloy particles.[10,12]

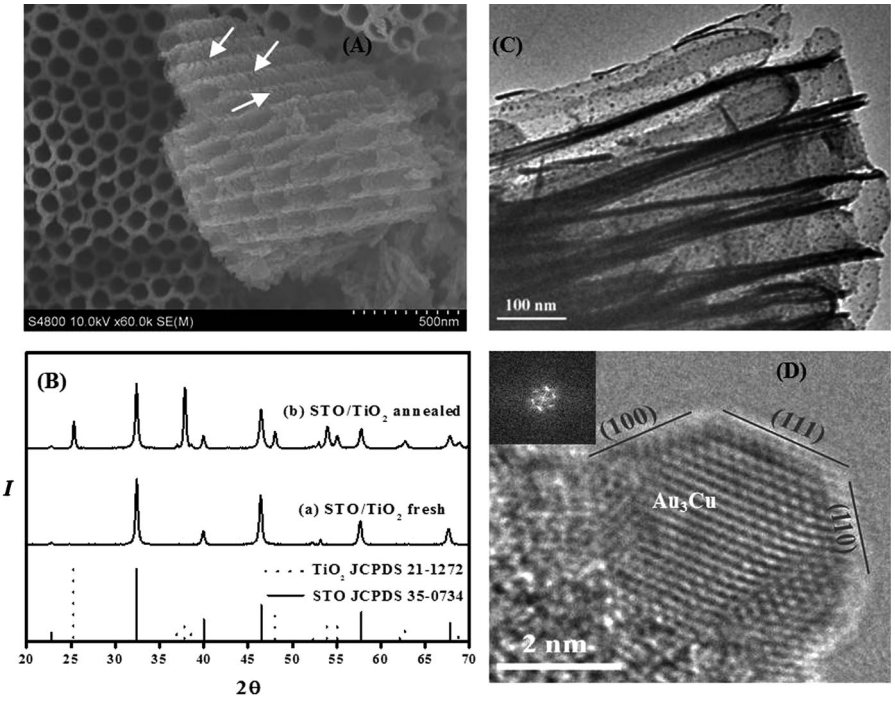

Figure 1. A) SEM image, the white arrows indicate the holes in the tube wall; B) XRD pattern of STO/TiO_2 nanotube arrays; C) TEM image of Au_3Cu@STO/TiO2 nanotube arrays; D) HRTEM image and FFT pattern of Au_3Cu nanoparticles.

Catalytic activity was tested for the photoreduction of CO_2. The reactions were performed by hanging a piece of photocatalyst film in 10 mL $N_2H_4{\cdot}H_2O$ or H_2O under a diluted CO_2 (33.3 % in Ar) atmosphere in the dark or under a Xe-lamp illumination. Figure 2 A shows the amount of CH_4 generated on the Au-Cu@STO/TiO_2 nanotube arrays by using $N_2H_4{\cdot}H_2O$ or H_2O as the H source and electron donor. The Au–Cu alloy co-catalysts exhibit much higher activity than Au and Cu owing to the alloying effect.[10,13] The increase in the fraction of Au in bimetallic alloy NPs enhances the photocatalytic activity, and the Au_3Cu@STO/TiO_2 nanotube arrays give the largest CH_4 evolution rate of 15.49 ppm $cm^{-2}\,h^{-1}$ (421.2 μmol $g^{-1}\,h^{-1}$). In contrast, the Au@STO/TiO_2 nanotube arrays and Cu@STO/TiO_2 nanotube arrays show lower activity of CH_4 evolution. The most

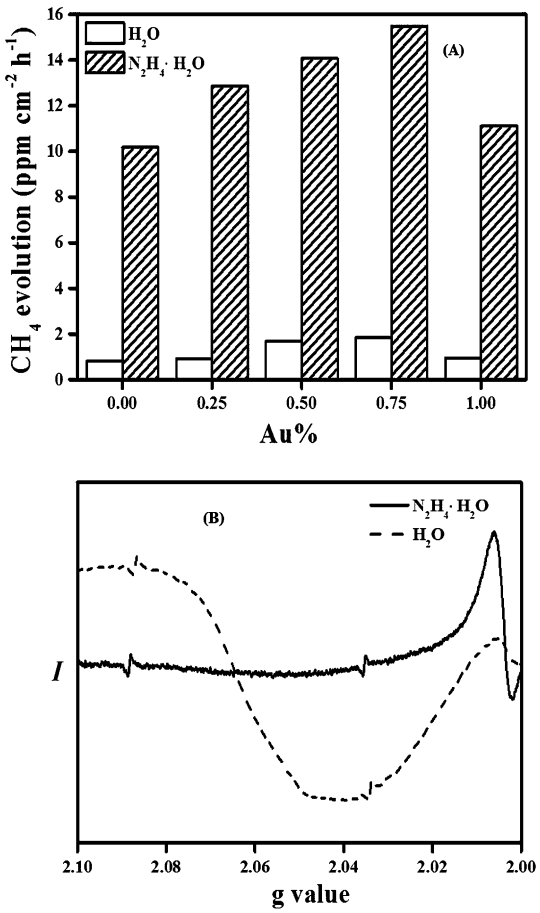

Figure 2. A) Amount of CH_4 formed during the photoreduction of CO_2 on Au-Cu@STO/TiO_2 nanotube arrays relative to the Au fraction in bimetallic alloy nanoparticles. B) ESR spectra of Au_3Cu@STO/TiO_2 nanotube arrays after the photoreduction reaction with $N_2H_4 \cdot H_2O$ and H_2O as H source and electron donor.

interesting feature of the alloy co-catalyst is the significant activity enhancement observed under $N_2H_4 \cdot H_2O$ protection. Although using H_2O as H source and electron donor, the Au-Cu NPs co-catalyst shows a similar alloy effect, it undergoes a rapid deactivation during the photocatalytic reaction (Figure S5), which is caused by surface oxidation of Cu atoms with photogenerated holes and oxygen species (such as ·OH, O_2)[10,14] and elimination of the alloying effects. The present result demonstrates that $N_2H_4 \cdot H_2O$ maintains the Au–Cu alloying effect and promotes CO_2 reduction without co-catalyst deactivation, which is confirmed by ESR analysis (Figure 2B). After the photoreduction process in H_2O vapor, an intense signal, which is assigned to Cu^{2+}, is observed at a g value of approximately 2.06,[10,14] indicating that surface Cu atoms are oxidized. On the contrary, exposure of the Au_3Cu@STO/TiO_2 nanotube array sample to $N_2H_4 \cdot H_2O$ leads to complete disappearance of the Cu^{2+} signal. This suggests that the oxidized surface Cu atoms are reduced by $N_2H_4 \cdot H_2O$, which guarantees a high photocatalytic activity for CO_2 reduction.

$N_2H_4 \cdot H_2O$ is widely considered as a promising hydrogen-storage material owing to its high content of hydrogen (7.9%) and it offering the advantage of CO-free H_2 production.[15] However, in contrast to the broad application of H_2O[5,16] and H_2[5,17] as reductants, a study using $N_2H_4 \cdot H_2O$ in a photocatalytic CO_2 reduction system has not been reported. The decomposition of hydrazine to H_2 and N_2 is confirmed in our experiments. Figure 3A shows a time-dependent change in the amount of total hydrocarbon, CH_4, CO, H_2, and N_2 formed by photoreduction of CO_2 on the Au_3Cu@STO/TiO_2 nanotube arrays catalyst under UV/Vis light illumination. The increases of released gas are plotted as a function of illumination time. A CO production rate of 138.6 ppm cm^{-2} h^{-1} (3.77 mmol g^{-1} h^{-1}) and total hydrocarbon production of 26.68 ppm cm^{-2} h^{-1} (725.4 μmol g^{-1} h^{-1}) are obtained under 6 h illumination. In the hydrocarbon production, CH_4 is the main product with an evolution rate of 15.49 ppm cm^{-2} h^{-1} (421.2 μmol g^{-1} h^{-1}), which is 60% of the total hydrocarbon products. The other hydrocarbons are C_2H_6, C_2H_4, and C_3H_6, which are identified by GC (Figure S6). The corresponding quantum efficiency for the photoreduction is 2.51%. After five cycles measurement during a 34 h test, the CH_4 gas-evolution rate decreases from 15.49 to 13.57 ppm cm^{-2} h^{-1}, which is still 87.6% of its original activity (Figure 3B). In addition, H_2, N_2, and all the reduction products increase continuously with increasing illumination time. This result indicates that the $N_2H_4 \cdot H_2O$ provides a strongly reductive atmosphere to maintain the effectiveness of the photocatalyst, which promises a long stability of the photocatalyst. This opens a feasible route to choose a reductant for CO_2 reduction, which also aids the development of the photocatalysts and co-catalysts.

To demonstrate the superiority of the nanoarchitecture, several control experiments were carried out and the result is shown in Figure 3C. The amounts of hydrocarbons formed on STO/TiO_2 coaxial nanotube arrays are much higher than that on the STO nanotube arrays and TiO_2 nanotube arrays. This result suggests that the STO/TiO_2 heterostructure can effectively separate the photogenerated carriers, promoting the photocatalytic activity. This conclusion is further supported by the photoelectrochemical (PEC) performance evaluation (Figure S7). Further loading with Au–Cu bimetallic alloy NPs causes a sharp increase in the reduction products. This demonstrates that the noble Au–Cu NPs help the redox process. In particular, CO becomes the main product of the reduction. The amount of hydrocarbons productions are in tens of ppm/cm^2 (which are multiplied by a factor of 10 in the Figure 3C). In contrast, the $Au_3 + Cu_1$@STO/TiO_2 plate-like catalyst prepared by a step-by-step deposition of Au and Cu metal onto the support exhibits much lower photoactivity. This means the nanotube array architecture can greatly increase the available surface area and provide specific geometric pathways for charge transport. The photocatalytic activity of Au_3Cu@STO/TiO_2 plate is 3.5 times higher than that of $Au_3 + Cu_1$@STO/TiO_2 plate which indicates that the homogeneously mixed Au–Cu NPs are necessary for the alloy effect. For Au–Cu@STO/TiO_2 nanotube arrays, the alloy effect plays an important role in improving the efficiency and determining the selectivity. As a result of the alloy effect caused by the homogeneously mixed Au–Cu atoms, the electron densities on Au–Cu alloy NPs are much higher than

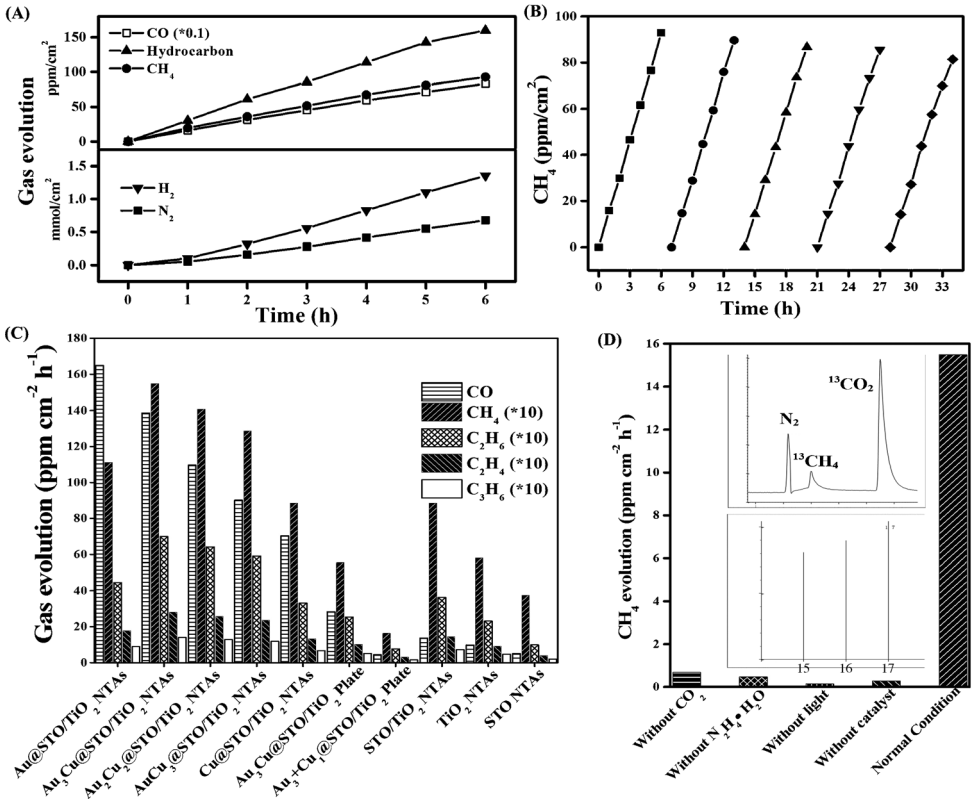

Figure 3. A) Gas-evolution rates as a function of illumination time. B) Cycling measurements of CH_4 generation on Au_3Cu@STO/TiO_2 nanotube arrays, each cycle is shown with a different symbol. C) Photocatalytic reduction products formed on various catalysts. D) CH_4 evolution in reference experiments. Inset: Gas chromatogram and mass spectrum of $^{13}CH_4$ (m/z 17, 16, and 15) produced over Au_3Cu@STO/TiO_2 nanotube arrays.

the single Au and Cu NPs.[10,13] Moreover, the alloy NPs can effectively restrain the reverse transportation of the accumulated photogenerated electrons to the semiconductors.[18] Hence, the Au–Cu alloy co-catalysts exhibit much higher activity than Au and Cu. The increase in the fraction of Au in bimetallic alloy NPs enhances the hydrocarbons production. However, unlike the hydrocarbons, the CO production increasing with the Au fraction does not follow the alloy effect. According to previous report, CO_2 is first deoxygenated to form CO, and then gradually reduced to CH_4 and other hydrocarbon fuels.[4a] Since the activation energy associated with the CO desorption is much lower on Au ($E_a = 38\ kJ\,mol^{-1}$)[19] than that on Cu ($E_a = 67\ kJ\,mol^{-1}$),[20] desorption of CO from the Au surface is kinetically favored. So the Au–Cu alloy co-catalysts with higher Au fraction show higher selectivity for CO formation. Considering the work function of Cu (4.65 eV) is less than Au (5.1 eV),[21] the photogenerated electrons prefer to move from the semiconductors (STO, TiO_2) to the Au atoms through the Schottky contact.[22] The interfacial charge transfer of the electrons from Au atoms to the electron acceptors (such as CO_2, CO) is much slower than the charge transfer between the inner, homogeneously mixed alloy, metal atoms.[18] These accumulated electrons on the Au atoms may rapidly transfer to the neighboring Cu atoms. Generally, Cu has been widely shown to be a highly active catalyst for CO reduction to form hydrocarbons.[20,23] In our case, Au–Cu alloy favors CO desorption from the Au atom and boosts the formation of hydrogenation species on the Cu atom. This might be the main reason why the Au–Cu alloy effect works for hydrocarbon species but not for the CO formation. The inferior activity of Cu@STO/TiO_2 nanotube arrays is probably caused by the low electron-donating ability of Cu,[10,12–14] which results in a lower electron density in the Cu@STO/TiO_2 nanotube arrays than in the Au@STO/TiO_2 nanotube arrays.

Figure 3D shows the CH_4 evolution rate when the reference experiments were carried out. When the experiment was performed in the absence of $N_2H_4{\cdot}H_2O$, catalyst, or light illumination, only a negligible amount of CH_4 was detected. Because there is trace CH_4 in the natural air, the CH_4 in the above-mentioned experiments is considered as contamination from the air during samplings. Nevertheless, when the diluted CO_2 (33.3 % in Ar) was replaced by pure Ar gas, a small amount of CH_4 was found which should be generated from the photoreduction of the remaining CO_2 on the sample surface.[24] In a normal-condition experiment using labeled $^{13}CO_2$ as the substrate lead to the formation of $^{13}CH_4$ (Inset in Figure 3D), showing that the CH_4 formed is indeed the product of CO_2 reduction. Consequently, all the above-mentioned reference experiments confirm that the $N_2H_4{\cdot}H_2O$ offers H atoms, CO_2 supplies as carbon source, and the photocatalyst provides the redox potentials for the whole reaction to finally produce CO, CH_4, and other hydrocarbons.

To investigate the mechanism of the CO_2 photoreduction, in situ FTIR experiments were carried out. As shown in Figure 4, a series adsorption bands around 1330–1590 cm^{-1} and 1600–1890 cm^{-1} appear under the UV/Vis irradiation, and their intensities increase with increasing irradiation time. The characteristic adsorption bands 1335–1560 cm^{-1} and 1610–1750 cm^{-1} are due to the bending vibration of C–H, the stretching vibration of C=O and the asymmetric stretching of O–C=O, which belong to the intermediate products, such as aldehydes, carboxylic acids, and bidentate carbonates.[25] The weak band at 1339 cm^{-1} is from the bending vibration of C–H in CH_4.[25] Since it is difficult to adsorb CH_4 molecules on the surface of the sample, the intensity of this adsorption band is rather low. According to the in situ FTIR

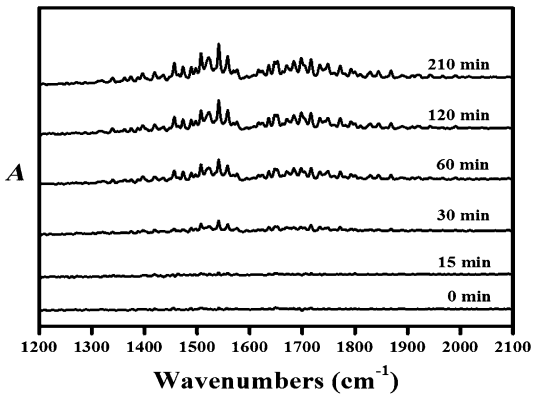

Figure 4. In situ FTIR spectra for CO_2 photoreduction on Au_3Cu@STO/TiO_2 nanotube arrays under full-arc Xe-lamp irradiation for different time.

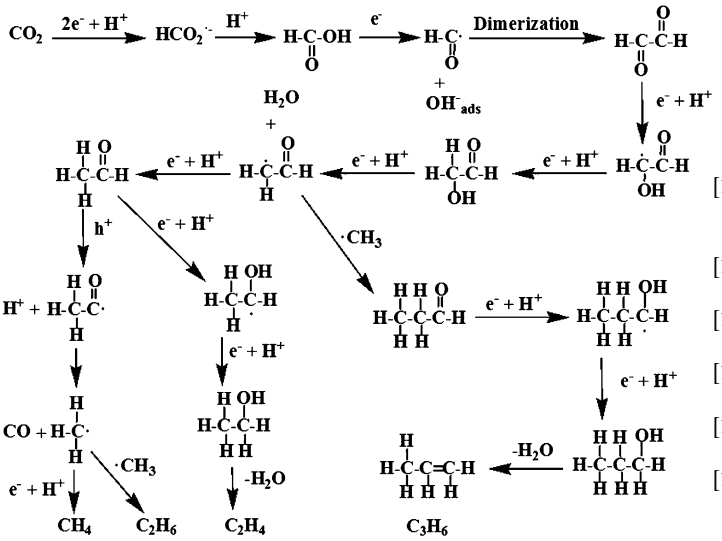

Scheme 1. The proposed mechanism for the photoreduction of CO_2. ads = adsorbed, h^+ = hole.

spectra results and the breaking of C–O bonds and creating of new C–H bonds they imply, we proposed the mechanism for the CO_2 photoreduction, as shown in Scheme 1, which is in agreement with the glyoxal pathway.[4a]

In summary, the results reported herein highlight the exploration of easily prepared STO/TiO_2 coaxial nanotube arrays. High CO and hydrocarbon generation rates were achieved by loading Au–Cu bimetallic alloy NPs onto these STO/TiO_2 coaxial nanotube arrays as effective catalysts for the photoreduction of CO_2. By varying the fraction of one component in this bimetallic alloy system, a Au_3Cu@STO/TiO_2 nanotube array has been found that is the most reactive photocatalyst in this family to generate hydrocarbons from diluted CO_2. $N_2H_4{\cdot}H_2O$, as the H source and electron donor, provides a reductive atmosphere for maintaining the alloying effect. This opens a feasible route to enhance the photocatalytic efficiency, which also aids the development of photocatalysts and co-catalysts.

Received: September 17, 2014
Published online: November 24, 2014

Keywords: Au-Cu cocatalyst · CO_2 conversion · nanotube arrays · photocatalysis · solar fuel

[1] S. C. Roy, O. K. Varghese, M. Paulose, C. A. Grimes, *Acs Nano* **2010**, *4*, 1259 – 1278.
[2] X. Zhang, F. Han, B. Shi, S. Farsinezhad, G. P. Dechaine, K. Shankar, *Angew. Chem. Int. Ed.* **2012**, *51*, 11778 – 11782; *Angew. Chem.* **2012**, *124*, 11948 – 11952.
[3] M. Halmann, *Nature* **1978**, *275*, 115 – 116.
[4] a) S. N. Habisreutinger, L. Schmidt-Mende, J. K. Stolarczyk, *Angew. Chem. Int. Ed.* **2013**, *52*, 7372 – 7408; *Angew. Chem.* **2013**, *125*, 7516 – 7557; b) K. F. Li, X. Q. An, K. H. Park, M. Khraisheh, J. W. Tang, *Catal. Today* **2014**, *224*, 3 – 12.
[5] Y. Izumi, *Coord. Chem. Rev.* **2013**, *257*, 171 – 186.
[6] J. Zhang, J. H. Bang, C. Tang, P. V. Kamat, *ACS nano* **2009**, *4*, 387 – 395.
[7] a) X. Wang, Z. Li, J. Shi, Y. Yu, *Chem. Rev.* **2014**, *114*, 9346 – 9384; b) Y. Li, X. Y. Yang, Y. Feng, Z. Y. Yuan, B. L. Su, *Crit. Rev. Solid State Mater. Sci.* **2012**, *37*, 1 – 74.
[8] a) X. Feng, J. D. Sloppy, T. J. LaTempa, M. Paulose, S. Komarneni, N. Bao, C. A. Grimes, *J. Mater. Chem.* **2011**, *21*, 13429 – 13433; b) O. K. Varghese, M. Paulose, T. J. LaTempa, C. A. Grimes, *Nano Lett.* **2009**, *9*, 731 – 737.
[9] R. M. Rioux, R. Komor, H. Song, J. D. Hoefelmeyer, M. Grass, K. Niesz, P. D. Yang, G. A. Somorjai, *J. Catal.* **2008**, *254*, 1 – 11.
[10] Y. Sugano, Y. Shiraishi, D. Tsukamoto, S. Ichikawa, S. Tanaka, T. Hirai, *Angew. Chem. Int. Ed.* **2013**, *52*, 5295 – 5299; *Angew. Chem.* **2013**, *125*, 5403 – 5407.
[11] R. K. de Richter, T. Z. Ming, S. Caillol, *Renewable Sustainable Energy Rev.* **2013**, *19*, 82 – 106.
[12] N. E. Motl, E. Ewusi-Annan, I. T. Sines, L. Jensen, R. E. Schaak, *J. Phys. Chem. C* **2010**, *114*, 19263 – 19269.
[13] W. Li, A. Wang, X. Liu, T. Zhang, *Appl. Catal. A* **2012**, *433*, 146 – 151.
[14] X. Liu, A. Wang, L. Li, T. Zhang, C. Y. Mou, J. F. Lee, *J. Catal.* **2011**, *278*, 288 – 296.
[15] a) L. He, Y. Huang, A. Wang, X. Wang, X. Chen, J. J. Delgado, T. Zhang, *Angew. Chem. Int. Ed.* **2012**, *51*, 3699 – 3702; *Angew. Chem.* **2012**, *124*, 3759 – 3762; b) H. L. Jiang, S. K. Singh, J. M. Yan, X. B. Zhang, Q. Xu, *ChemSusChem* **2010**, *3*, 541 – 549.
[16] Q. Zhai, S. Xie, W. Fan, Q. Zhang, Y. Wang, W. Deng, Y. Wang, *Angew. Chem. Int. Ed.* **2013**, *52*, 5776 – 5779; *Angew. Chem.* **2013**, *125*, 5888 – 5891.
[17] F. Sastre, A. Puga, L. Liu, A. Corma, H. García, *J. Am. Chem. Soc.* **2014**, *136*, 6798.
[18] R. Su, R. Tiruvalam, A. J. Logsdail, Q. He, C. A. Downing, M. T. Jensen, N. Dimitratos, L. Kesavan, P. P. Wells, R. Bechstein, *ACS Nano* **2014**, *8*, 3490 – 3497.
[19] J. Gottfried, K. Schmidt, S. Schroeder, K. Christmann, *Surf. Sci.* **2003**, *536*, 206 – 224.
[20] I. Bönicke, W. Kirstein, S. Spinzig, F. Thieme, *Surf. Sci.* **1994**, *313*, 231 – 238.
[21] S. Trasatti, *J. Electroanal. Chem.* **1972**, *39*, 163 – 184.
[22] R. Marschall, *Adv. Funct. Mater.* **2014**, *24*, 2421 – 2440.
[23] M. D. Porosoff, J. G. G. Chen, *J. Catal.* **2013**, *301*, 30 – 37.
[24] a) N. M. Dimitrijevic, B. K. Vijayan, O. G. Poluektov, T. Rajh, K. A. Gray, H. He, P. Zapol, *J. Am. Chem. Soc.* **2011**, *133*, 3964 – 3971; b) H. Zhou, J. Guo, P. Li, T. Fan, D. Zhang, J. Ye, *Sci. Rep.* **2013**, *3*, 1 – 9.
[25] T. Wang, X. Meng, P. Li, S. Ouyang, K. Chang, G. Liu, Z. Mei, J. Ye, *Nano Energy* **2014**, *9*, 50 – 60.

